

Astronomical pacing of late Palaeocene to early Eocene global warming events

Lucas J. Lourens¹, Appy Sluijs², Dick Kroon³, James C. Zachos⁴, Ellen Thomas⁵, Ursula Röhl⁶, Julie Bowles⁷ & Isabella Raffi⁸

At the boundary between the Palaeocene and Eocene epochs, about 55 million years ago, the Earth experienced a strong global warming event, the Palaeocene–Eocene thermal maximum^{1–4}. The leading hypothesis to explain the extreme greenhouse conditions prevalent during this period is the dissociation of 1,400 to 2,800 gigatonnes of methane from ocean clathrates^{5,6}, resulting in a large negative carbon isotope excursion and severe carbonate dissolution in marine sediments. Possible triggering mechanisms for this event include crossing a threshold temperature as the Earth warmed gradually⁷, comet impact⁸, explosive volcanism^{9,10} or ocean current reorganization and erosion at continental slopes¹¹, whereas orbital forcing has been excluded¹². Here we report a distinct carbonate-poor red clay layer in deep-sea cores from Walvis ridge¹³, which we term the Elmo horizon. Using orbital tuning, we estimate deposition of the Elmo horizon at about 2 million years after the Palaeocene–Eocene thermal maximum. The Elmo horizon has similar geochemical and biotic characteristics as the Palaeocene–Eocene thermal maximum, but of smaller magnitude. It is coincident with carbon isotope depletion events in other ocean basins, suggesting that it represents a second global thermal maximum. We show that both events correspond to maxima in the ~405-kyr and ~100-kyr eccentricity cycles that post-date prolonged minima in the 2.25-Myr eccentricity cycle, implying that they are indeed astronomically paced.

Biotic phenomena similar to those characterizing the Palaeocene–Eocene thermal maximum (PETM) have been locally recorded in the upper Palaeocene to lower Eocene, indicating the possibility of additional hyperthermal events, though of smaller magnitude^{14–16}. Several short, negative carbon isotope shifts of up to 1‰ at deep-sea sites resemble the much larger-amplitude carbon isotope excursion at the PETM¹². Orbital tuning suggested that these transients were controlled by maxima in the short-term eccentricity cycles, whereas the PETM carbon isotope excursion allegedly occurred near a minimum in the ~405-kyr eccentricity cycle, excluding orbital forcing as a triggering mechanism for the latter¹².

One objective of Ocean Drilling Program (ODP) Leg 208 on the Walvis ridge (subtropical southeastern Atlantic Ocean) was to search for hyperthermal events within the lower Cenozoic greenhouse climate record. We recovered continuous, undisturbed lower Palaeogene successions at five sites along a 2-km water depth transect in multiple (mostly advanced piston core) holes. This resulted in the first complete early Palaeogene deep-sea record accumulated at

relatively high sedimentation rates¹³. The uppermost Palaeocene and lower Eocene are composed of foraminifer-bearing nannofossil ooze, with a few chert layers and two deep-red clay layers marking the PETM and a younger distinctive horizon, named Elmo. Magneto-stratigraphic results on Site 1262 (see Supplementary Information) reveal that the Elmo horizon at 117.1–117.2 m composite depth (m.c.d.) is slightly older than the chron C24r/C24n reversal boundary (115–116 m.c.d.) (Supplementary Fig. 1) and occurs within the lower part of NP11.

The Elmo horizon is 10–15 cm thick, and characterized by elevated magnetic susceptibility (MS) values at all sites (Fig. 1). Analysis of the CaCO₃ content (expressed in weight per cent: wt%) of the deepest Site 1262 (palaeodepth¹³, 3,600 m), intermediate Site 1266 (palaeodepth, 2,600 m) and shallowest Site 1263 (palaeodepth, 1,500 m) reveal that the increase in MS is linearly related to a drop in CaCO₃ wt% (Supplementary Fig. 2). The CaCO₃ wt% declines from 90–95 below, to ~40 within, the red clay. High-resolution bulk carbon isotope records ($\delta^{13}\text{C}_{\text{bulk}}$) of Sites 1262, 1265, 1266 and 1267 reveal a negative excursion of 1.0–1.2‰ from below the first decline in CaCO₃ wt% into the Elmo (Fig. 1). The $\delta^{13}\text{C}_{\text{bulk}}$ of Site 1263 shows the largest depletion (1.4–1.6‰), suggesting that the red clay layer at this site with the highest sedimentation rate¹³ is stratigraphically the most complete and/or least affected by the dissolution of primary calcite and the presence of reworked or secondary calcite. The post-Elmo interval mirrors the typical PETM signature with an exponential recovery to pre-excursion $\delta^{13}\text{C}_{\text{bulk}}$ values. The bulk carbonate oxygen isotope record ($\delta^{18}\text{O}_{\text{bulk}}$) of Site 1263 shows a negative excursion of ~1.6‰ (Fig. 2).

From Site 1263, we analysed the stable isotopic composition of individual specimens (>300 μm size fraction) of the surface-dwelling planktonic foraminifer *Acarinina soldadoensis* and the benthic foraminifers *Cibicides* spp. and *Anomalinoidea* spp. (Fig. 2). The planktonic foraminiferal data show a much larger inter-specimen variability within each sample (especially within the Elmo horizon) than the benthic data. The (smoothed) carbon isotope record of *A. soldadoensis* ($\delta^{13}\text{C}_{A.\text{soldadoensis}}$) resembles the pattern of the bulk record, but shows a significantly larger negative excursion (~2.5‰). The carbon isotope shift is much smaller in the benthic foraminiferal record than in *A. soldadoensis*, but the (~1‰) trend through the carbonate-rich intervals equals that of the bulk and planktonic isotope records. Benthic foraminifera species richness is low and assemblages are dominated by diminutive *Nuttallides truempyi* and *Abyssamina* spp. species in the Elmo horizon. The

¹Faculty of Geosciences, Department of Earth Sciences, and ²Laboratory of Palaeobotany and Palynology, Department of Palaeoecology, Utrecht University, Budapestlaan 4, 3584 CD Utrecht, The Netherlands. ³Faculty of Earth and Life Sciences, Vrije Universiteit, De Boelelaan 1085, 1081 HV Amsterdam, The Netherlands. ⁴Earth Science Department, University of California, Santa Cruz, Earth and Marine Sciences Building, Santa Cruz, California 95064, USA. ⁵Department of Earth and Environmental Sciences, Wesleyan University, 265 Church Street, Middletown, Connecticut 06459-0139, USA, and Center for the Study of Global Change, Department of Geology and Geophysics, Yale University, PO Box 208109, New Haven, Connecticut 06520-8109, USA. ⁶DFG Research Center for Ocean Margins (RCOM), University of Bremen, Leobener Strasse, 28359 Bremen, Germany. ⁷Scripps Institution of Oceanography, University of California, San Diego, 9500 Gilman Drive, MC0208, La Jolla, California 92093, USA. ⁸Facoltà di Scienze, Dipartimento Scienze della Terra, Università "G. d'Annunzio" di Chieti, Campus Universitario Madonna delle Piane, Via dei Vestini 31, 66013 Chieti Scalo, Italy.

Supplementary Information

This file contains six supplementary figures, additional references, and extended description of methods used and discussion on (1) magnetobiostratigraphy, (2) magnetic susceptibility (MS) and CaCO_3 weight% scales shown in Figure 1, (3) spectral results and astronomical phase relations and (4) global significance of the ETM2 event (and *Elmo* horizon).

Magnetobiostratigraphy

Discrete samples were taken from the working half cores of Site 1262 in 8 cm³ cubes. Samples were alternating field (AF) demagnetised in steps up to 60 mT, using the “double-demagnetisation” technique¹ for AF levels above 30 mT. A drilling overprint was generally removed by 15 mT, and the remanence direction was calculated by principle component analysis² for steps from 20 to 40 mT (4 to 6 points). Directions with a maximum angular deviation² >10° were rejected. The remaining inclinations were used—along with shipboard pass-through data—to determine polarity.

The new magnetostratigraphic interpretation reveals that the *Elmo* horizon at 117.1–117.2 meters composite depth (mcd) occurs below the C24r/C24n reversal boundary at 115–116mcd (Supplementary Fig. 1) and not above as it was initially interpreted based on the shipboard measurements³ alone. The shipboard data are noisy, presumably resulting from a combination of low magnetisation and some drilling and/or splitting related deformation. While the discrete data generally give results consistent with the shipboard results, a notable exception is Hole 1262C, on which the shipboard interpretation was largely based. In this case, the discrete samples—taken from the centre of the cores—are presumed to be less deformed than the whole core, therefore giving more reliable data. In addition, a closer examination of records indicated that the first section in Core 1262C-3H was disturbed (highlighted in Supplementary Figure 1), providing unreliable pass-through data. Taken together, discrete and pass-through data from Hole 1262B and the discrete data from Hole 1262C confine the reversal to the interval between 115–116 mcd. The Hole 1262A data show a more gradual transition, but over an interval consistent with that seen in the other holes.

The new magnetostratigraphic interpretation is confirmed by the 20cm-spaced high-resolution calcareous nannofossil biostratigraphy we established for Site 1262. The NP10/NP11⁴ (CP9a/CP9b⁵) boundary was observed at 118.5 ± 0.1 mcd, where the crossover in abundance between *Tribrachiatus contortus* and *T. orthostylus* is present. Other events which are related to the base of NP11 and maintain the same relative stratigraphic positions are from old to young: top of *Discoaster multiradiatus* at 119.6 ± 0.1 mcd, and the first occurrences of *Sphenolithus radians* and *T. orthostylus* at 118.5 ± 0.1 mcd. This shows that NP10/NP11 (CP9a/CP9b) is positioned below the C24r/C24n reversal (and *Elmo* horizon), in accordance with the magnetobiostratigraphic results obtained from previous DSDP holes drilled at Walvis Ridge⁶. Furthermore, the lowermost occurrence of *T. orthostylus* was found at 295.75 ± 0.45 mcd in Site 1263, 282.25 ± 0.75 mcd in Site 1265, 295.89 ± 0.45 mcd in Site 1266, 208.35 ± 0.75 mcd in Site 1267, all confirming that the *Elmo* horizon is younger than the NP10/NP11 boundary.

Magnetic susceptibility and CaCO₃ weight% scales

The high-resolution MS/g records of Holes 1262A, 1263C, and 1266C were compared to the split core point magnetic susceptibility (PMS) and whole core MS of the multiple sensor track (MS-MST) measurements obtained during Leg 208³. We choose to convert all MS data to the MS-MST scale by performing linear regression analyses between MS/g and PMS (Supplementary Fig. 2a) and the conversion of PMS to MS-MST using the equation $MST = PMS \times 2.0683 + 7.8257$ ($R^2 = 0.99$)³. Subsequently, a regression analysis between the CaCO₃ weight% and the MS/g (converted to the MS-MST scale) of the same samples was applied (Supplementary Fig. 2b) to obtain the estimated CaCO₃ weight% scale of the various sites (Fig. 1).

Spectral results and astronomical tuning procedure

Power spectra were obtained by using the CLEAN transformation⁷ and the Blackman-Tukey method⁸. For the determination of errors associated with the frequency spectra of the CLEAN algorithm, we applied a Monte Carlo based method⁹. Significance levels of 95, 97.5, 99 and 99.5% for the Monte Carlo spectra of the MS and L* depth series were determined by 1) 10% (i.e., Control parameter = 0.1) white noise addition, 2) Clean Gain factor of 0.1, 3) 500 CLEAN Iterations, 4) dt value of 0.02m, and 5) a total number of simulation iterations of 1000. The Blackman-Tukey power spectra were obtained by using the AnalySeries 1.1 software package¹⁰. In this case, data sets were equally spaced and prepared by removing the linear trends. Bandwidths of ~0.19 (Site 1262) and ~0.16 (Site 1267) have been applied as window to smooth the various spectra of the depth series.

The CLEAN^{7,9} modulus and Blackman-Tukey^{8,10} power spectra of L* and MS for Site 1262 revealed consistent and significant peaks at ~510, 123, 53, 38, 30 and 24.5cm (Supplementary Fig. 3). This frequency distribution of the spectral peaks is in good agreement with that of the astronomical cycles: the periodicities of these cycles equal 96 (short eccentricity), 41.5 (obliquity), 30 (obliquity), 23.5 (precession) and 19.5kyr (precession), respectively, if the ~510cm cycle is a reflection of the 405kyr¹¹ (long) eccentricity period. This assumption is consistent with the shipboard age model, which resulted in an average sedimentation rate for the early Eocene time interval at Site 1262 of ~1.2cm/kyr³. The correlative depth interval at Site 1267 revealed significant peaks in the L* spectra at ~570, and 146cm, and to a lesser degree at 58, and 32cm. The long and short eccentricity cycles thus appear to dominate the spectral distribution of this record, whereas the reflection of the obliquity and precession-related cycles is weak and diffuse.

To illustrate how we established the astronomical phase relationship for the extracted short and long eccentricity related MS and L* of Sites 1262 and 1267 (Fig. 3), a detail of the lithological changes in the interval just above the PETM of Site 1262 is shown in Supplementary Fig. 4. This interval clearly reflects the regular occurrence of pink coloured layers (p), which are repeatedly grouped in distinctive bundles of 2-3 layers. The 25-30cm spacing of successive pink coloured layers within one bundle corresponds to the precession-related spectral peaks (Supplementary Fig. 3), indicating that these layers are precession-forced. Evidently, the bundles are related to the short eccentricity-related MS maxima and are more frequently present during the long eccentricity-related MS maxima. In analogy to the well-known astronomical phase relations for the late

Neogene Mediterranean sapropel (=organic-enriched layer) record¹²⁻¹⁴, the bundling of pink coloured layers should correspond to a maximum in eccentricity. Due to the eccentricity modulation of the climatic precession cycle, this orbital configuration should have lead to amplified seasonal contrasts on both Hemispheres and hence climate change, thereby triggering the deposition of the pink coloured layers, although it is yet not clear whether these layers should correspond to precession minima or maxima. The near absence of these layers during the long eccentricity-related MS minima further implies that these periods should correspond to minima in the ~405kyr eccentricity cycle, that weakens the effect of the ~100kyr modulation on climatic precession, and hence reduces the precessional-driven seasonal contrasts on both Hemispheres.

To investigate whether the very long orbital variations of ~2.25Myr have had an effect on the amplitude changes of the short eccentricity cycles between the PETM and *Elmo* horizon we extracted the ~100kyr component from the L* and MS records of Site 1262 by using a Gaussian filter centred at a frequency of 0.8125 ± 0.1 per meter (Supplementary Fig. 5). This analysis clearly revealed that the amplitude changes of the ~100kyr cycles are on-average less amplified during the second (II) ~405kyr related cycle of the L* and MS records from Site 1262 (Fig. 3). This spectral characteristic was compared with the minimum amplitude changes in the ~100kyr eccentricity cycles derived from R7¹⁵ and La2004¹¹ orbital solutions using a Gaussian filter centred at a frequency of 0.0095 ± 0.002 per kyr (Supplementary Fig. 5). Subsequently, the extracted short and long eccentricity related components of the L* and MS records from Site 1262 were tuned using the most likely combination of both the ~2.25Myr related amplitude changes in the ~100kyr cycle and ~405kyr cycle (Fig. 3).

Global significance of the ETM2 event (and *Elmo* horizon)

To illustrate the global significance of the ETM2 event we compared our high-resolution $\delta^{13}\text{C}_{\text{bulk}}$ records across the *Elmo* horizon (this study) and PETM¹⁶ of Site 1262 with those obtained from the subtropical Northwest Atlantic ODP Site 1051 and the high-latitude Southern Ocean ODP Site 690¹⁷ (Supplementary Fig 6). These sites revealed a relatively strong negative excursion (termed H1) just below C24n/C24r (Site 1051) and within NP11 (Sites 690 and 1051), which bears strong resemblance with a similar negative excursion in the North Atlantic DSDP Site 550, and equatorial Pacific DSDP Site 577¹⁷ (not shown). Given the good magnetobiostratigraphic constraints as well as the relative strength of this carbon isotope excursion with respect to that of the PETM, we conclude that the H1 is the equivalent of the ETM2 event. It should be noted that of all these sites only the magnetobiostratigraphy of Site 690 seems questionable, probably due to a series of unconformities immediately above the transient event H1 as indicated by the tight succession of the NP10/NP11, NP11/NP12, and NP12/NP14 zonal boundaries¹⁸⁻²⁰.

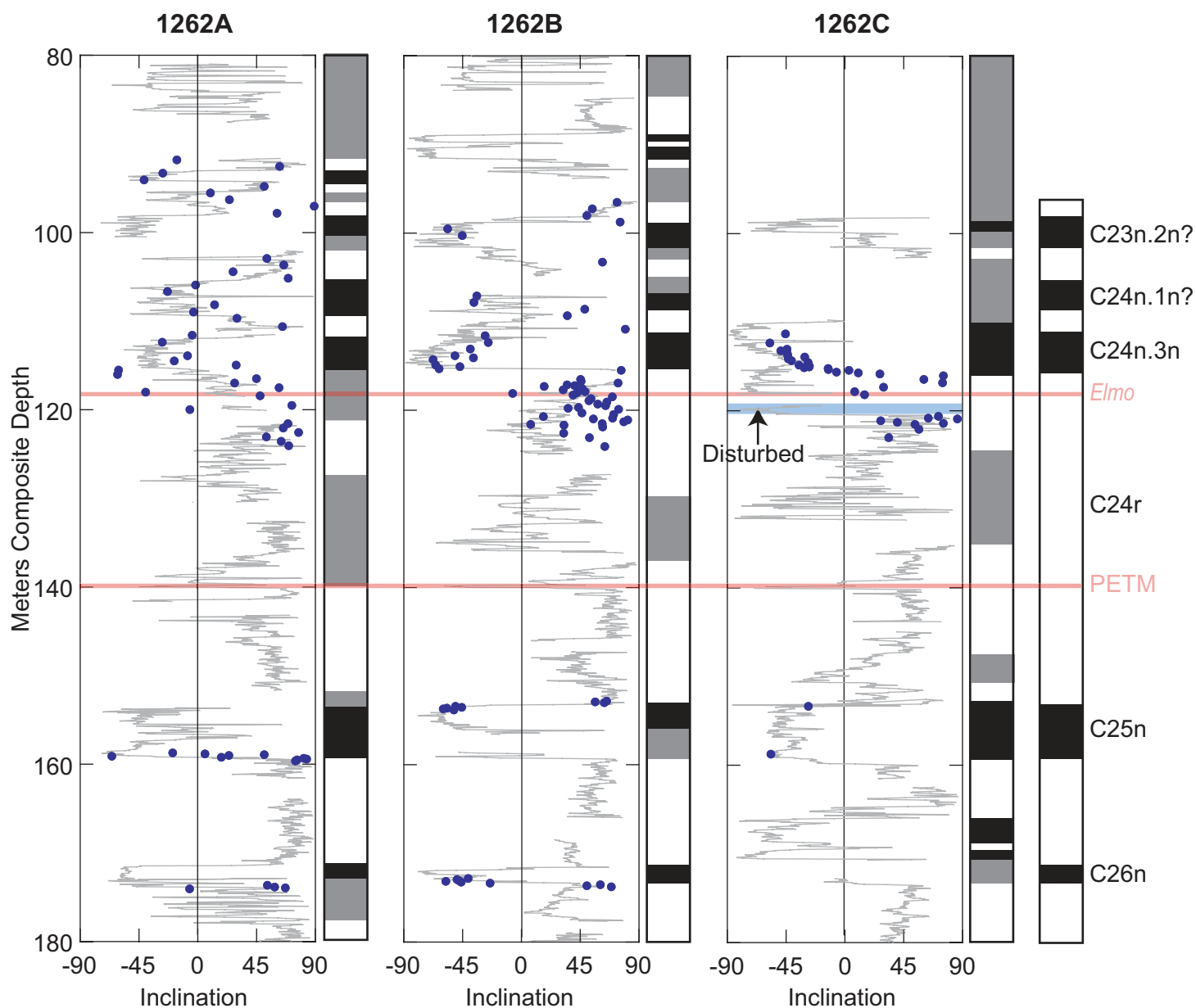
To further illustrate that the CIE associated with the ETM2 is not only recorded in the marine realm, we also plotted the paleosol soil nodule carbonate isotope record from the Bighorn Basin²¹ in Supplementary Fig. 6. Although this record seems to reflect a noisy signal in some parts, the application of a 3 point moving average clearly demonstrate that the long-term Eocene $\delta^{13}\text{C}$ low is superimposed by two excursions: one definitely

related to the PETM and the other less amplified excursion in the interval just below the C24n/r boundary to, most likely, the ETM2 event.

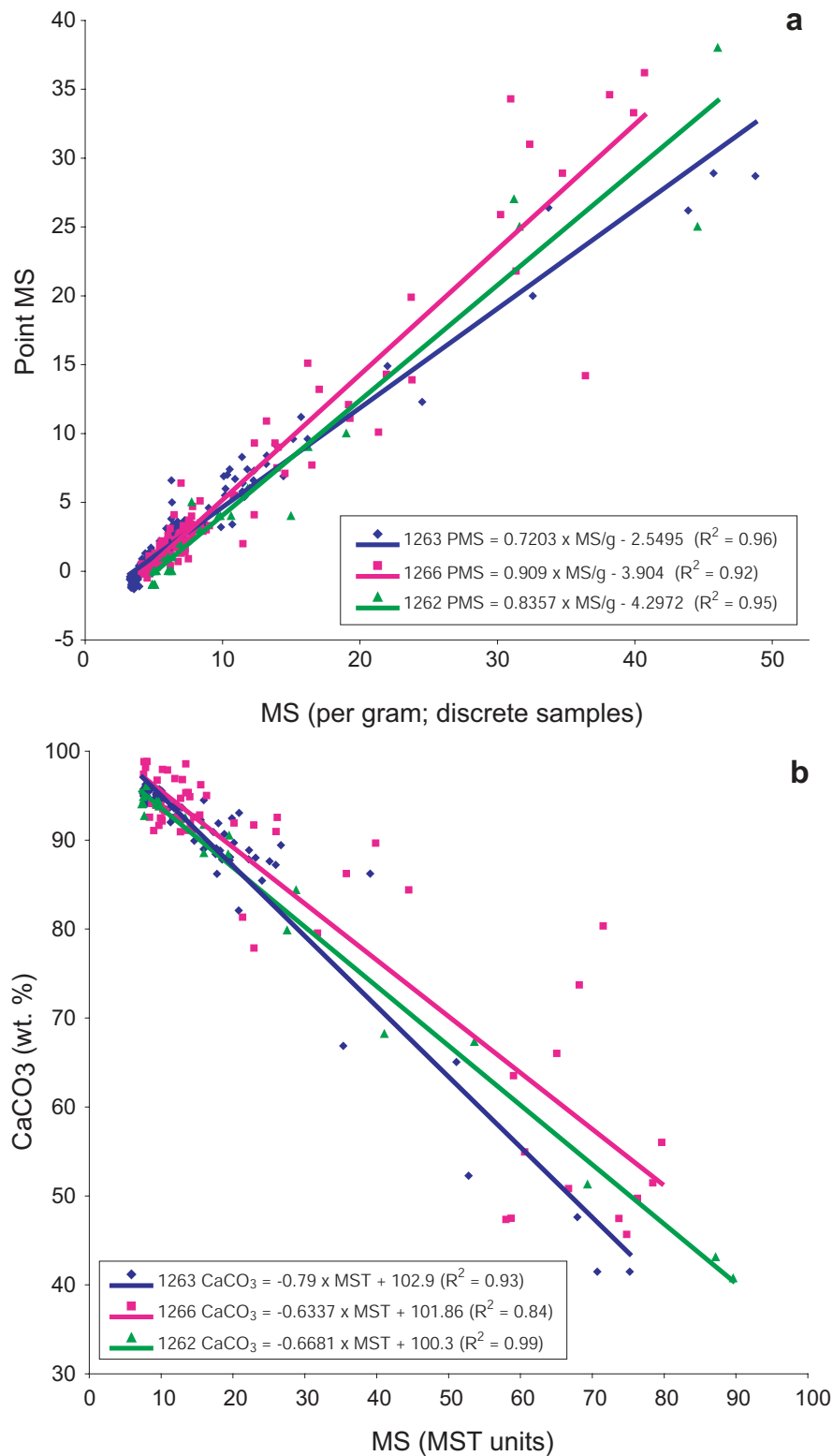
References

1. Tauxe, L., Pick, T. & Kok, Y. S. Relative paleointensity in sediments: a pseudo-Thellier approach. *Geophysical Research Letters* **22**, 2885-2888 (1995).
2. Kirschvink, J. L. The least-squares line and plane and the analysis of paleomagnetic data. *Geophys. J. Roy. Astron. Soc.* **62**, 699-718 (1980).
3. Zachos, J. C., Kroon, D., Blum, P. & al., e. *Early Cenozoic Extreme Climates: The Walvis Ridge Transect* (eds. Zachos, J. C., Kroon, D. & Blum, P.) (2004).
4. Martini, E. in *Planktonic Conference* (ed. Farinacci, A.) 739-785 (Tecnosci, Roma, 1971).
5. Okada, H. & Bukry, D. Supplementary modification and introduction of code numbers to the low-latitude coccolith biostratigraphic zonation (Bukry, 1973; 1975). *Mar. Micropaleontol.* **5**, 321-325 (1980).
6. Backman, J. Late Paleocene to middle Eocene calcareous nannofossil biochronology from Shatsky Rise, Walvis Ridge and Italy. *Palaeo Geography Climatology Ecology* **57**, 43-59 (1986).
7. Roberts, D. H., Lehar, J. & Dreher, J. W. Time series analysis with CLEAN. Part I. Derivation of a spectrum. *Astron. J.* **93**, 968-989 (1987).
8. Blackman, R. B. & Tukey, J. W. *The Measurement of Power Spectra From the Point of View of Communication Engineering*. (Dover Publications, New York, 1958).
9. Heslop, D. & Dekkers, M. J. Spectral analysis of unevenly spaced climatic time series using CLEAN: signal recovery and derivation of significance levels using a Monte Carlo simulation. *Physics of the Earth and Planetary Interiors* **130**, 103-116 (2002).
10. Paillard, D., Labeyrie, L. & Yiou, P. Macintosh Program Performs Time-Series Analysis. *Eos Trans. AGU* **77**, 379 (1996).
11. Laskar, J. et al. A long term numerical solution for the insolation quantities of Earth. *Astronomy and Astrophysics* **428**, 261-285 (2004).
12. Hilgen, F. J. Astronomical calibration of Gauss to Matuyama sapropels in the Mediterranean and implication for the geomagnetic polarity time scale. *Earth Planet. Sci. Lett.* **104**, 226-244 (1991).
13. Lourens, L. J. et al. Evaluation of the Plio-Pleistocene astronomical timescale. *Paleoceanography* **11**, 391-413 (1996).
14. Hilgen, F. J. et al. Extending the astronomical (polarity) time scale into the Miocene. *Earth Planet. Sci. Lett.* **136**, 495-510 (1995).
15. Varadi, F., Bunnegar, B. & Ghil, M. Successive refinements in long-term integrations of planetary orbits. *Astrophysical J.* **592**, 620-630 (2003).
16. Zachos, J. C. et al. Rapid Acidification of the Ocean during the Paleocene-Eocene Thermal Maximum. *Science* (in press).
17. Cramer, B. S., Wright, J. D., Kent, D. V. & Aubry, M.-P. Orbital climate forcing of $\delta^{13}\text{C}$ excursions in the late Paleocene–early Eocene (chrons C24n–C25n). *Paleoceanography* **18**, 10.1029/2003PA000909 (2003).

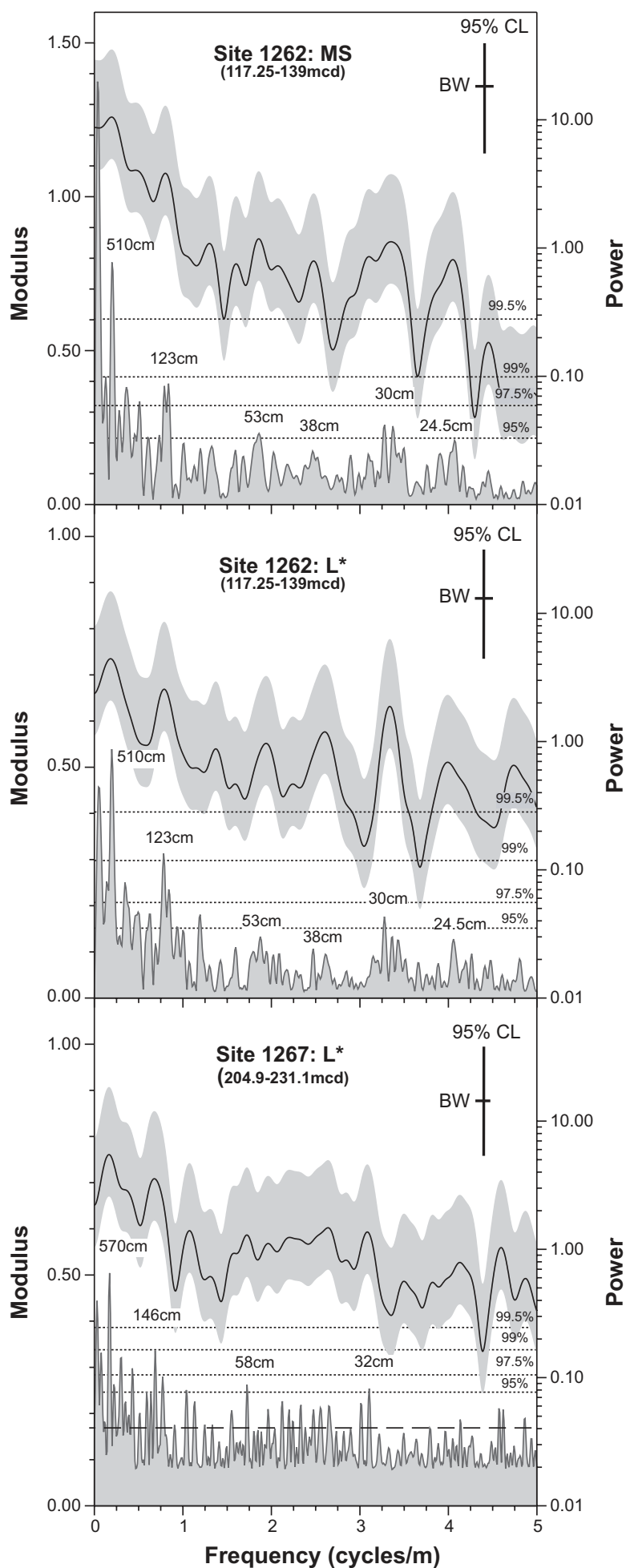
18. Berggren, W. A. & Aubry, M.-P. in *Correlation of the Early Paleogene in Northwest Europe, Special Publication* (eds. Knox, R. W. O. B., Corfield, R. M. & Dunay, R. E.) (Geol. Soc., London, 1996).
19. Aubry, M.-P., Berggren, W. A., Stott, L. D. & Sinha, A. in *Correlation of the Early Paleogene in Northwest Europe, Special Publication* (eds. Knox, R. W. O. B., Corfield, R. M. & Dunay, R. E.) (Geol. Soc., London, 1996).
20. Ali, J., Kent, D. V. & Hailwood, E. Magnetostratigraphic reinvestigation of the Palaeocene/Eocene boundary interval in Hole 690B, Maud Rise. *Geoph. J. Int.* **141**, 639-646 (2000).
21. Koch, P. L. et al. in *Causes and Consequences of Globally Warm Climates in the Early Paleogene* (eds. Wing, S. L., Gingerich, P. D., Schmitz, B. & Thomas, E.) 49-64 (Geological Society of America Special Paper, Boulder, Colorado, 2003).



Supplementary Figure 1 Late Palaeocene to early Eocene magnetostratigraphy for ODP Site 1262. Shipboard pass-through inclination (demagnetized to 15 mT; grey lines) and discrete sample inclination (principle component calculated from 20 to 40 mT; blue circles). Shaded interval on site 1262C represents a particularly disturbed core section, results from which should not be considered reliable. Overall magnetostratigraphic interpretation to right. Black = normal polarity; white = reverse; grey = indeterminate.

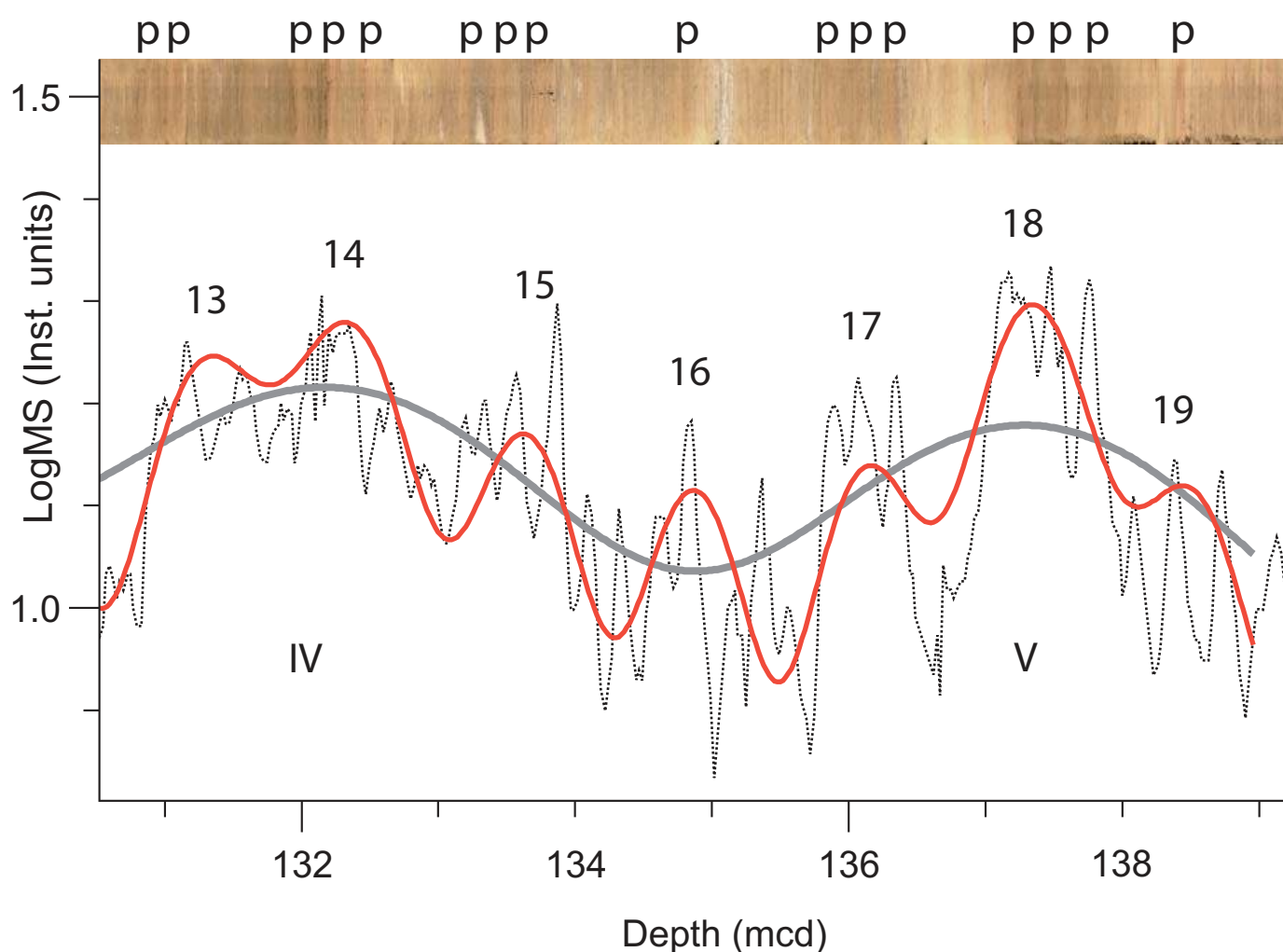


Supplementary Figure 2 Regression analyses for the magnetic susceptibility to calcium carbonate weight percentage conversion of Sites 1262, 1263 and 1267. **a**, Magnetic susceptibility per gram sediment (MS/g) versus shipboard point magnetic susceptibility (PMS). The MS/g values were converted to the shipboard magnetic susceptibility scale of the multi sensor track (MS-MST) using the displayed function for each site and the equation $\text{MS-MST} = \text{PMS} \times 2.0683 + 7.8257$ ($R^2 = 0.99$) (Ref. 3). **b**, MS/g (on the recalibrated MS-MST scale) versus CaCO₃ weight%.

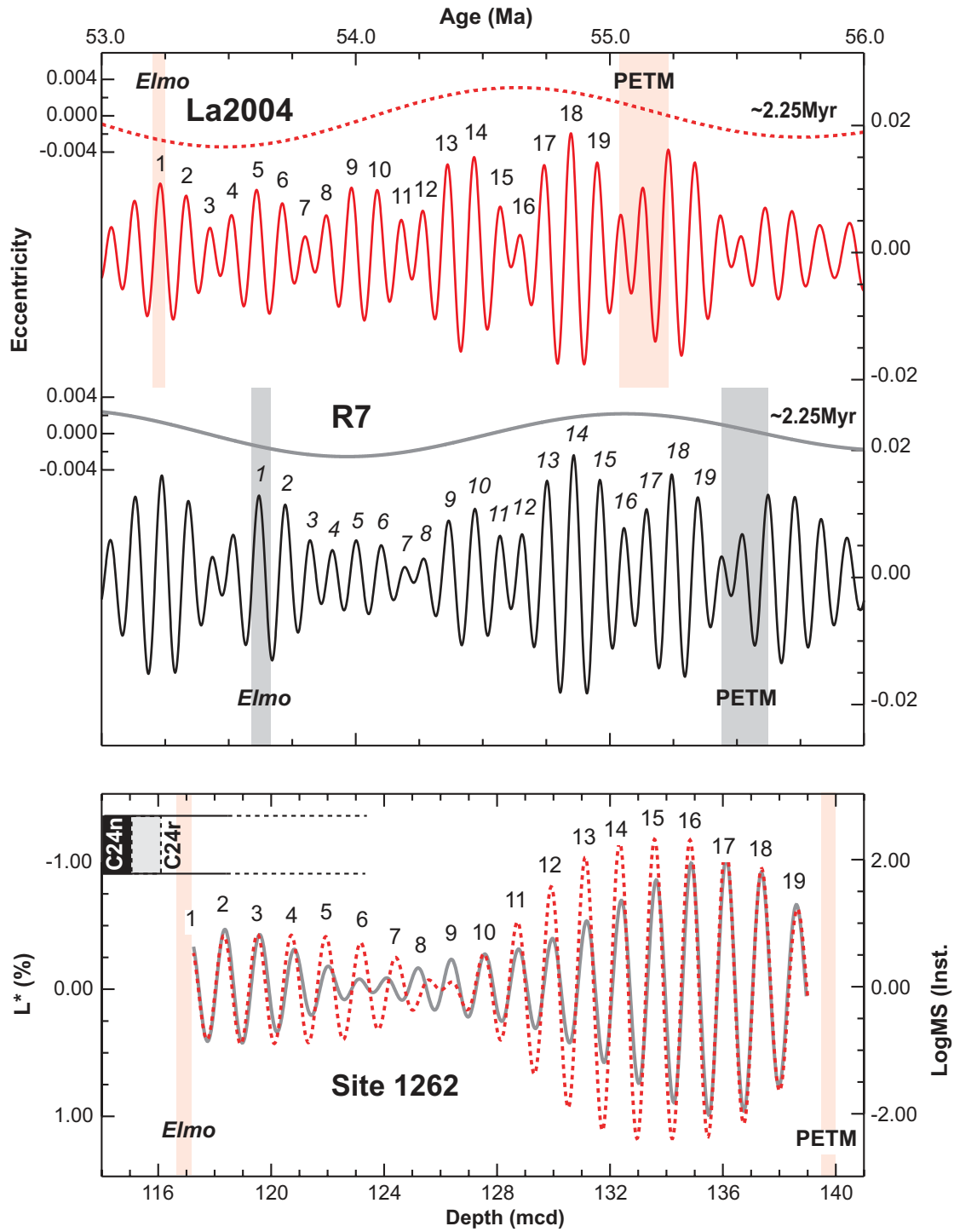


Supplementary Figure 3 Frequency spectra of the magnetic susceptibility and color reflectance records of Sites 1262 and 1267 for the *Elmo*-PETM interval. Results of the CLEAN-algorithm and Blackman-Tukey (BT) are expressed by their modulus and power, respectively. Horizontal dotted lines indicate the 95, 97.5, 99, and 99.5% significance level of the CLEANED-spectra. Bandwidth (BW) and 95% confidence limits (CF) of the BT spectra are based on a Tukey window with a number of lags that equal 30% the length of the data series.

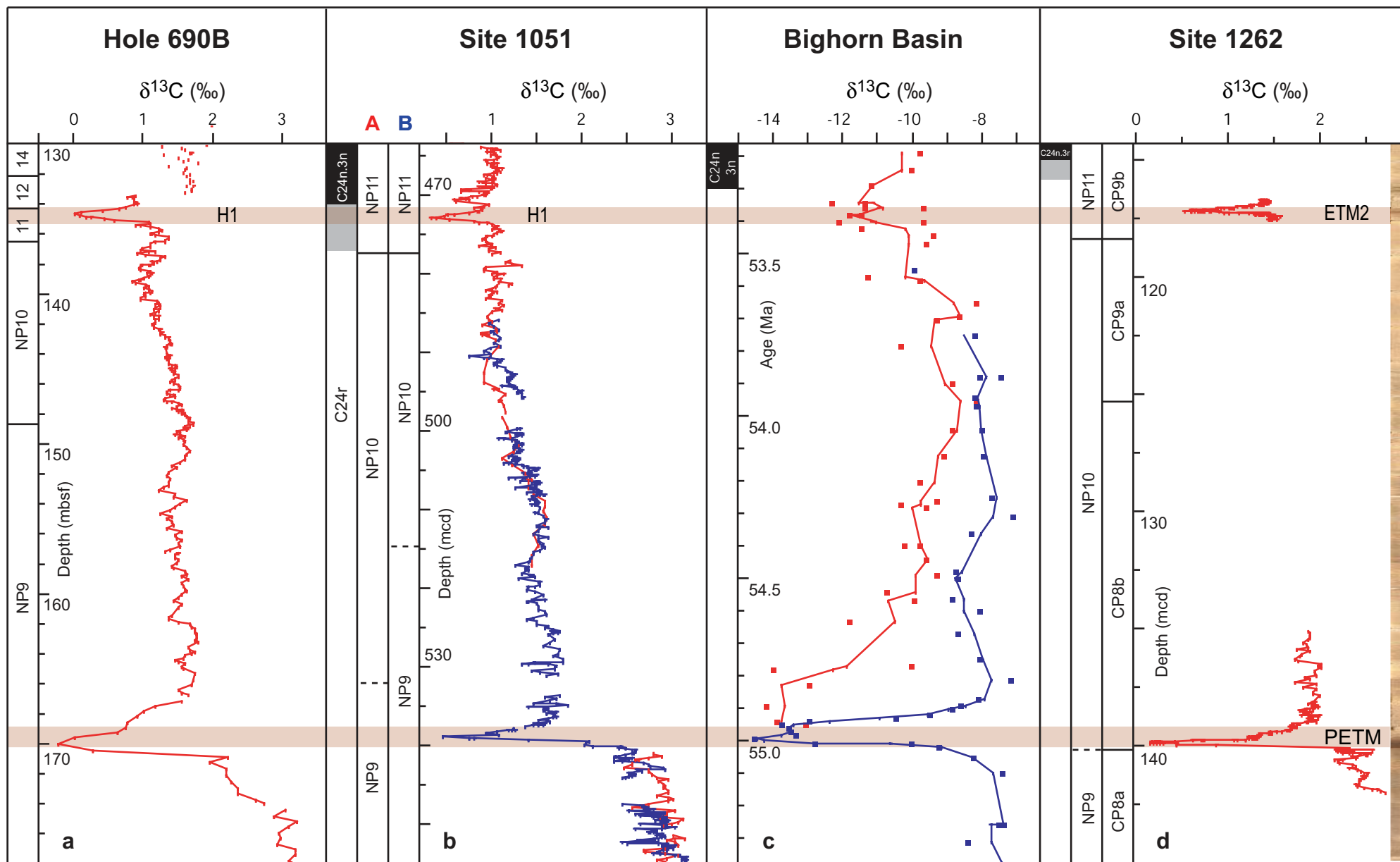
Site 1262



Supplementary Figure 4 Comparison between precession-related lithological changes and eccentricity cycles in the magnetic susceptibility record of Site 1262. The pink-coloured layers, related to precession, are particularly distinctive during maxima in the short and long-term eccentricity related cycles of the MS record.



Supplementary Figure 5 Amplitude modulation of the ~100kyr eccentricity components in Site 1262 and orbital computations. Gaussian filters centred at a frequency of 0.0095 ± 0.002 per kyr and 0.8125 ± 0.1 per meter were applied to extract the ~100kyr eccentricity components from the R7 (Ref. 15) and La2004 (Ref. 11) orbital solutions and their correlative cycles from the L^* (solid) and MS (dot) records of Site 1262, respectively.



Supplementary Figure 6 Global registration of the PETM and *Elmo* carbon isotope excursions in four well-dated (magneto- and/or nannofossil stratigraphy) sections. **a**, ODP Hole 690B (Southern Ocean) (Ref. 17). **b**, ODP Holes 1051A (red) and 1051B (blue) (Blake Nose, Northwestern Atlantic) (Ref. 17). **c**, Paleosol carbonate isotope record from the Bighorn Basin (Wyoming, USA) (Ref. 21). **d**, ODP Site 1262 (this study) and PETM (Ref. 16).

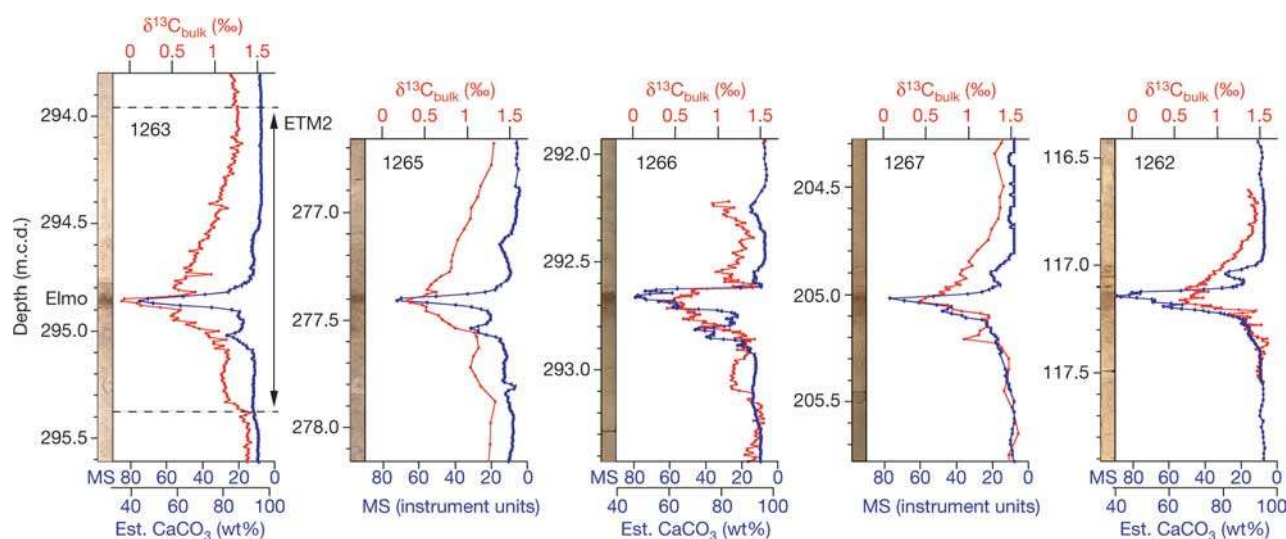


Figure 1 | Bulk carbonate $\delta^{13}\text{C}$ and magnetic susceptibility (MS) records across the Elmo horizon at five ODP Leg 208 sites. The CaCO_3 wt% axes are estimates based on linear correlation with MS measurements on the same samples (Methods). Site numbers are given at the top left of each panel.

Site numbers and water depths (m) are as follows: 1263, 2,717 m; 1265, 3,060 m; 1266, 3,798 m; 1267, 4,355 m; 1262, 4,755 m. Digital images of the lithology are plotted at the left site of each panel.

few measured benthic isotope values of the Elmo horizon, representing *Anomalinoidea* spp. specimens (*Cibicidoides* spp. >300 μm are absent in the Elmo horizon), are similar to those from outside the clay layer, indicating that these are probably derived from bioturbated specimens. This suggests that large-sized benthic foraminifera were absent during deposition of the Elmo horizon, as commonly observed for the PETM¹⁷. The presence of light-coloured burrows within the red clay layer documents bioturbation, and could explain the scatter in the planktonic isotope values, and the less strong $\delta^{13}\text{C}_{\text{bulk}}$ excursion relative to $\delta^{13}\text{C}_{A.\text{soldadoensis}}$. This possibility does not rule out that the magnitude of the excursion in the deep sea could have been damped owing to the larger carbon mass of this reservoir. The maximum oxygen isotope shift in *A. soldadoensis* ($\delta^{18}\text{O}_{A.\text{soldadoensis}}$) across the Elmo horizon is comparable to that of the $\delta^{18}\text{O}_{\text{bulk}}$ record. There is only a $\sim 0.6\text{‰}$ shift in the benthic

oxygen isotope record, either because no *in situ* large benthic foraminifera are present in the Elmo horizon or changes in bottom water temperatures were minor.

To unravel the orbital relationship between the Elmo horizon and PETM, we studied the cyclic sedimentary patterns of the interlying interval in continuous spliced cores derived from advanced piston core holes only. Spectral analysis was applied on the colour reflectance (L^*) of Site 1267, and L^* and MS of Site 1262 (see Supplementary Information). The spectra of all records revealed the dominance of the long ($\sim 405\text{-kyr}$) and short ($\sim 100\text{-kyr}$) eccentricity cycles (Supplementary Fig. 3). Both components were extracted and could be unambiguously correlated between the records of these sites (Fig. 3). Four long-term maxima in MS (minima in L^*) occur between the Elmo horizon and PETM. The Elmo horizon corresponds to a fifth long-term MS maximum (L^* minimum) and a

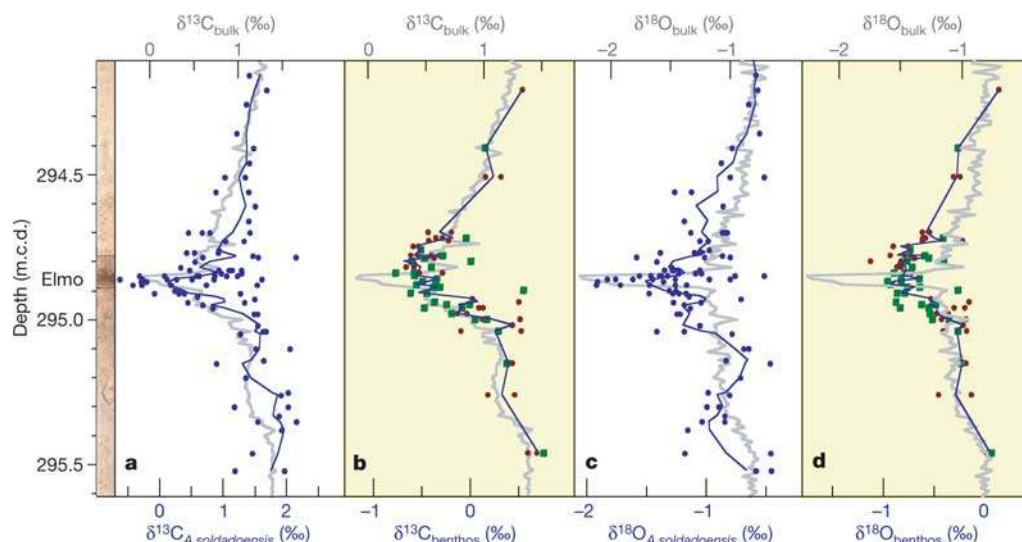


Figure 2 | Stable isotope series of bulk sediment and single foraminifer specimens across the Elmo horizon at Site 1263. **a**, The $\delta^{13}\text{C}$ values (blue dots) of the surface dwelling planktonic foraminifer *A. soldadoensis* ($\delta^{13}\text{C}_{A.\text{soldadoensis}}$). **b**, The $\delta^{13}\text{C}$ values of the bottom dwelling benthic foraminifers ($\delta^{13}\text{C}_{\text{benthos}}$) *Cibicidoides* spp. (red squares) and *Anomalinoidea* spp. (green dots). **c** and **d** as in **a** and **b** but for $\delta^{18}\text{O}$. Grey lines in **a** and **b**, and in **c** and **d**, indicate respectively the $\delta^{13}\text{C}$ and $\delta^{18}\text{O}$ values of the bulk sediment ($\delta^{13}\text{C}_{\text{bulk}}$, $\delta^{18}\text{O}_{\text{bulk}}$). Blue lines represent three-point moving averages on averaged values of duplicate analyses of a sample.

spp. (green dots). **c** and **d** as in **a** and **b** but for $\delta^{18}\text{O}$. Grey lines in **a** and **b**, and in **c** and **d**, indicate respectively the $\delta^{13}\text{C}$ and $\delta^{18}\text{O}$ values of the bulk sediment ($\delta^{13}\text{C}_{\text{bulk}}$, $\delta^{18}\text{O}_{\text{bulk}}$). Blue lines represent three-point moving averages on averaged values of duplicate analyses of a sample.

short-term MS maximum (L^* minimum) cycle. The red clay layer associated with the PETM ends in a long-term MS minimum (L^* maximum). If there were 11 climate precession cycles in the PETM interval¹⁸, then its carbon isotope excursion corresponds to a maximum (minimum) in the long-term MS (L^*) cycle, similar to the Elmo.

A definite tuning of the early Eocene to astronomical computations is complicated, because the precision of the orbital solution more than 45 Myr ago is limited^{19,20}. Tuning is in principle possible for the 405-kyr eccentricity cycle, because of its longer duration of stability^{19,20} (Fig. 3). At 50 Myr ago, the absolute uncertainty in time is about 20 kyr (ref. 20), but this did not lead to an astronomically

tuned timescale owing to large uncertainties in radiometric age constraints for this time interval²¹. A second uncertainty derives from the chaotic behaviour of the inner planets related to the resonant argument $\theta = (s_4 - s_3) - 2(g_4 - g_3)$, where g_3, g_4 are related to the precession of the perihelion and s_3, s_4 to the precession of the node of Earth and Mars²⁰. This causes a large uncertainty in the determination of the time when the relatively stable ~ 2.4 -Myr beat in eccentricity evolved from the ~ 1.2 -Myr period when $(s_4 - s_3) - (g_4 - g_3) = 0$ (that is, ~ 2.25 Myr in the nominal La2004²⁰ and R7¹⁹ solutions between 53–57 Myr ago). This problem limits an accurate age determination of successive minima in this very long eccentricity cycle and the related intervals of reduced amplitude

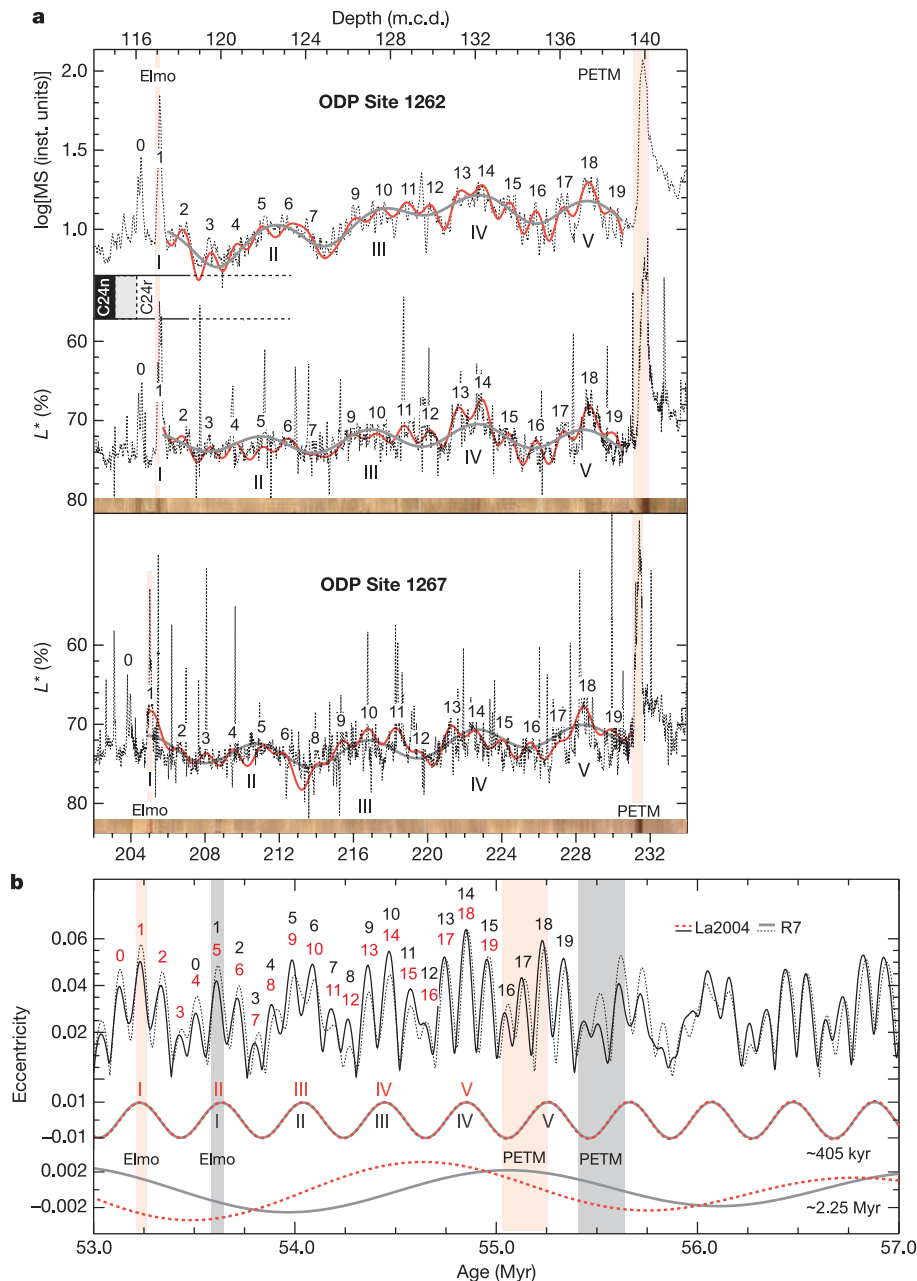


Figure 3 | Astronomical tuning of the lower Eocene sediments at Walvis ridge to two different orbital computations. **a**, The extracted short (red lines) and long (grey lines) eccentricity-related cycles from magnetic susceptibility (MS) and colour reflectance (L^*) of sites 1262 and 1267 (dashed lines) represent respectively the 97.5% and 99.5% significant peaks in the CLEAN spectra (Supplementary Fig. 4). **b**, Correlation of the long-

term (I–V) and short-term (0–19) eccentricity-related maxima to their correlative cycles in the R7²³ (grey) and La2004²⁴ (red) orbital solutions. The 405-kyr and ~ 2.25 -Myr cycles of eccentricity were extracted using a gaussian filter with a frequency of 0.00247 ± 0.0001 (kyr^{-1}) and of 0.00043 ± 0.0001 (kyr^{-1}), respectively.

changes in the short eccentricity cycle, and explains the offset between the ~ 2.25 -Myr cycles of the nominal La2004 and R7 solutions in the studied time interval (Fig. 3).

Because of these uncertainties, only a floating tuning could be realized (see also Supplementary Information). First, we emphasize that MS maxima (L^* minima) correlate to eccentricity maxima based on the distinct amplification of the precession-related lithological changes during the long- and short-term MS maxima (Supplementary Fig. 4). This observation is crucial, because it implies that the carbon isotope shifts associated with the PETM and Elmo horizon also correspond to maxima in the long and short eccentricity cycles (Fig. 3). Second, we correlated the (on average less amplified) ~ 100 -kyr cycles within the second (II; Fig. 3) ~ 405 -kyr cycle to the minimum in the ~ 2.25 -Myr cycle at 53.5 Myr ago (La2004) or 54.0 Myr ago (R7) (Supplementary Fig. 5). Using this first order calibration, we tuned all long and short eccentricity cycles, implying that all cycles should be shifted one ~ 405 -kyr cycle older in R7 than in the nominal La2004 solution (Fig. 3). As a result, the Elmo horizon correlates with the short eccentricity maximum at ~ 53.235 Myr ago (La2004) or ~ 53.620 Myr ago (R7), and the onset of the PETM carbon isotope excursion correlates with the long eccentricity maximum centred at ~ 55.270 Myr ago (La2004) or ~ 55.675 Myr ago (R7). This tuning implies that both events occurred briefly after a period of low-amplitude, short eccentricity changes associated with a minimum in the very long-term orbital perturbation of ~ 2.25 Myr.

The $\delta^{13}\text{C}_{\text{bulk}}$ negative shift of 1.4–1.6‰ in the Elmo horizon at Site 1263 is, with exception of the PETM carbon isotope excursion, of an unusually large magnitude for the early Palaeogene¹². Its position just below C24n/C24r and within NP11 suggests that this excursion correlates to the $\sim 1\%$ depletion characterizing the H1 event in the North Atlantic (DSDP Site 550 and ODP Site 1051), the Southern Ocean (ODP Site 690) and the Pacific Ocean (DSDP Site 577)¹² (see Supplementary Information). Moreover, the palaeosol carbonate isotope record from the Bighorn basin also shows a strong negative $\delta^{13}\text{C}$ excursion just below C24n/C24r²², indicating that the carbon isotope excursion is global and recorded in both marine and terrestrial basins (Supplementary Fig. 6). The Elmo horizon, however, has yet not been recognized at other locations, although the H1 event is accompanied by high MS values at Sites 550 and 690¹². Hence, the large drop in CaCO_3 wt% in the Walvis ridge cores probably indicates a major global ocean lysocline shoaling, but in contrast to the PETM²³, the calcite compensation depth appears to have remained below the palaeodepth of Site 1262. Application of the empirical temperature– $\delta^{18}\text{O}$ relationship^{24,25} indicates furthermore that the $\sim 1\%$ $\delta^{18}\text{O}_{\text{A.soldadoensis}}$ change within the Elmo horizon reflects a sea surface temperature rise of at least 3–4 °C, about half of the mid- to high-latitude sea surface temperature changes estimated for the PETM²⁶. All this suggests that the Elmo horizon characterizes a second pronounced early Eocene thermal maximum (ETM2; Fig. 1), similar to the PETM in both orbital and biogeochemical aspects, but of approximately half its amplitude in carbon isotope excursion, rise in sea surface temperature, and carbonate dissolution.

The linkage of both events to a similar orbital configuration disagrees with Cramer *et al.*¹², who related the PETM to a minimum and H1 (ETM2 equivalent) to a maximum in a ~ 405 -kyr cycle, thereby promoting the comet impact hypothesis⁸. In addition, according to their tuning the interval between the PETM carbon isotope excursion and C24n/C24r should span ~ 1.5 Myr, which is significantly shorter than the five ~ 405 -kyr cycles (~ 2 Myr) that we found. These discrepancies can probably be attributed to large uncertainties in their approach of using low-amplitude bulk carbon isotope transient excursions and counts of poorly expressed lithological cycles from incomplete successions¹². Hence, we suggest that the extreme seasonal contrast at both hemispheres during eccentricity maxima increased intermediate seawater temperatures,

thereby triggering the release of oceanic methane hydrates. In this respect, the critical conjunction of short, long and very long eccentricity cycles and the long-term late Palaeocene to early Eocene warming trend may have favoured the build-up of a significant methane hydrate reservoir before its release during both events, thereby excluding unique mechanisms for explaining the PETM^{5–11,27}. The less extreme signal of ETM2 may reflect the inability of the methane hydrate reservoir to return to pre-PETM dimensions, especially under the warm conditions that prevailed in the interval spanning the two events¹. Above ETM2 (H1) an increasing number of low-amplitude carbon transients occurred, of which the first, H2¹², seems to correspond with the two thin brown layers one 100-kyr cycle above the Elmo horizon (number 0 in Fig. 3), suggesting that the threshold for dissociation of clathrates was low during the early Eocene climatic optimum¹, enabling even the short eccentricity cycles to trigger minor methane releases.

METHODS

Sampling and CaCO_3 wt% analyses. Discrete sediment samples were collected at a 0.5–1-cm spacing across the Elmo horizon in holes 1262A, 1263C and 1266C. All samples were freeze-dried and analysed for magnetic susceptibility per gram sediment (MS g^{-1}) using an AGICO KLY-3 device. These records were compared to the split core point magnetic susceptibility (PMS) and whole core MS of the multiple sensor track (MS-MST) measurements obtained during Leg 208¹³. We converted all MS data to the MS-MST scale by performing linear regression analyses between MS g^{-1} and PMS (Supplementary Fig. 2) and the conversion of PMS to MS-MST using the equation $\text{MST} = (\text{PMS} \times 2.0683) + 7.8257$ ($R^2 = 0.99$)¹³.

Every fourth sample (but all within the Elmo horizon) was used for calcium carbonate analyses. The CaCO_3 wt% was based on the amount of total carbon combusted with the Fison NA 1500 CNS analyser. Analytical precision and accuracy were determined by comparison with an international standard (BCR-71) and in-house standards (F-TURB, MM-91). The relative standard deviations, analytical precision and accuracy were better than 3%. Several samples prepared for palynological studies revealed that no significant amount of organic carbon was present, with an uncertainty smaller than the analytical precision. A regression analysis between the CaCO_3 wt% and the MS g^{-1} (converted to the MS-MST scale) was applied (Supplementary Fig. 2) to obtain the estimated CaCO_3 wt% scale (Fig. 1).

Stable isotopes. Bulk stable isotope measurements were carried out for all sites with an average spacing of 4 cm, but in 0.5–1-cm resolution through the Elmo horizon. The isotope measurements were carried out using an ISOCARB common bath carbonate preparation device linked on-line to a VG SIRA24 mass spectrometer. Isotope values were calibrated to the Pee Dee Belemnite (PDB) scale. Analytical precision was determined by replicate analyses and by comparison to international (IAEA-CO1 and NBS19) and in-house (NAXOS) carbonate standards, showing standard deviations of $<0.06\%$ and $<0.1\%$ for $\delta^{13}\text{C}$ and $\delta^{18}\text{O}$, respectively.

Stable isotope measurements of individual planktonic and benthic foraminiferal specimens were carried out using a CARBO-KIEL automated carbonate preparation device linked on-line to a Finnigan MAT252 mass spectrometer. Specimens were hand picked from the $>300\ \mu\text{m}$ fraction and cleaned in ethanol in an ultrasonic bath for 30 s. Calibration to the international carbonate standard NBS19 revealed an analytical precision better than 0.03‰ and 0.05‰ for $\delta^{13}\text{C}$ and $\delta^{18}\text{O}$, respectively.

Received 17 November 2004; accepted 10 May 2005.
Published online 8 June 2005.

1. Zachos, J. C., Pagani, M., Sloan, L. C., Thomas, E. & Billups, K. Trends, rhythms, and aberrations in global climate 65 Ma to present. *Science* **292**, 686–693 (2001).
2. Norris, R. D. & Röhl, U. Carbon cycling and chronology of climate warming during the Palaeocene/Eocene transition. *Nature* **401**, 775–778 (1999).
3. Kennett, J. P. & Stott, L. D. Abrupt deep-sea warming, palaeoceanographic changes and benthic extinctions at the end of the Palaeocene. *Nature* **353**, 225–229 (1991).
4. Koch, P. L., Zachos, J. C. & Gingerich, P. D. Correlation between isotope records in marine and continental carbon reservoirs near the Palaeocene/Eocene boundary. *Nature* **358**, 319–322 (1992).
5. Dickens, G. R., O'Neil, J. R., Rea, D. K. & Owen, R. M. Dissociation of oceanic methane hydrate as a cause of the carbon isotope excursion at the end of the Paleocene. *Paleoceanography* **10**, 965–971 (1995).
6. Dickens, G. R., Castillo, M. M. & Walker, J. C. G. A blast of gas in the latest

- Paleocene: Simulating first-order effects of massive dissociation of oceanic methane hydrate. *Geology* **25**, 259–262 (1997).
7. Thomas, E. & Shackleton, N. J. in *Correlation of the Early Paleogene in Northwestern Europe* (eds Knox, R. W. O. B., Corfield, R. M. & Dunay, R. E.) 401–441 (Special Publication 101, Geological Society, London, 1996).
 8. Kent, D. V. *et al.* A case for a comet impact trigger for the Paleocene/Eocene thermal maximum and carbon isotope excursion. *Earth Planet. Sci. Lett.* **211**, 13–26 (2003).
 9. Bralower, T. J. *et al.* High-resolution records of the late Paleocene thermal maximum and circum-Caribbean volcanism: Is there a causal link? *Geology* **25**, 963–966 (1997).
 10. Schmitz, B. *et al.* Basaltic explosive volcanism, but no comet impact, at the Paleocene-Eocene boundary: high-resolution chemical and isotopic records from Egypt, Spain and Denmark. *Earth Planet. Sci. Lett.* **225**, 1–17 (2004).
 11. Katz, M. E., Cramer, B. S., Mountain, G. S., Katz, S. & Miller, K. G. Uncorking the bottle: What triggered the Paleocene/Eocene thermal maximum methane release? *Paleoceanography* **16**, 1–14 (2001).
 12. Cramer, B. S., Wright, J. D., Kent, D. V. & Aubry, M.-P. Orbital climate forcing of $\delta^{13}\text{C}$ excursions in the late Paleocene–early Eocene (chons C24n–C25n). *Paleoceanography* **18**, doi:10.1029/2003PA000909 (2003).
 13. Zachos, J. C., *et al.* in *Early Cenozoic Extreme Climates: The Walvis Ridge Transect* (eds Zachos, J. C., Kroon, D. & Blum, P.) (Ocean Drilling Program, College Station, Texas, 2004).
 14. Thomas, E. & Zachos, J. C. Was the late Paleocene thermal maximum a unique event? *Geol. Föhr. Stockh. Föhr. [Trans. Geol. Soc. Stockholm]* **122**, 169–170 (2000).
 15. Bujak, J. P. & Brinkhuis, H. in *Late Paleocene - Early Eocene Biotic and Climatic Events in the Marine and Terrestrial Records* (eds Aubry, M.-P., Lucas, S. G. & Berggren, W. A.) 277–295 (Columbia Univ. Press, New York, 1998).
 16. Röhl, U., Norris, R. D. & Ogg, J. G. in *Causes and Consequences of Globally Warm Climates in the Early Paleogene* (eds Wing, S. L., Gingerich, P. D., Schmitz, B. & Thomas, E.) 567–589 (Special Paper 369, Geological Society of America, Boulder, Colorado, 2003).
 17. Thomas, E., Zachos, J. C. & Bralower, T. J. in *Warm Climates in Earth History* (eds Huber, B. T., MacLeod, K. & Wing, S. L.) 132–160 (Cambridge Univ. Press, Cambridge, 2000).
 18. Röhl, U., Bralower, T. J., Norris, G. & Wefer, G. New chronology for the late Paleocene thermal maximum and its environmental implications. *Geology* **28**, 927–930 (2000).
 19. Varadi, F., Bunnegar, B. & Ghil, M. Successive refinements in long-term integrations of planetary orbits. *Astrophys. J.* **592**, 620–630 (2003).
 20. Laskar, J. *et al.* A long term numerical solution for the insolation quantities of Earth. *Astron. Astrophys.* **428**, 261–285 (2004).
 21. Machlus, M., Hemming, S. R., Olsen, P. E. & Christie-Blick, N. Eocene calibration of geomagnetic polarity time scale reevaluated: Evidence from the Green River Formation of Wyoming. *Geology* **32**, 137–140 (2004).
 22. Koch, P. L. *et al.* in *Causes and Consequences of Globally Warm Climates in the Early Paleogene* (eds Wing, S. L., Gingerich, P. D., Schmitz, B. & Thomas, E.) 49–64 (Special Paper 369, Geological Society of America, Boulder, Colorado, 2003).
 23. Zachos, J. C. *et al.* Rapid acidification of the ocean during the Paleocene-Eocene Thermal Maximum. *Science* (in the press).
 24. O'Neil, J. R., Clayton, R. N. & Mayeda, T. K. Oxygen isotope fractionation in divalent metal carbonates. *J. Chem. Phys.* **51**, 5547–5558 (1969).
 25. Shackleton, N. J. Oxygen isotope analyses and Pleistocene temperatures reassessed. *Nature* **215**, 15–17 (1967).
 26. Zachos, J. C. *et al.* A transient rise in tropical sea surface temperature during the Paleocene-Eocene thermal maximum. *Science* **302**, 1151–1154 (2003).
 27. Svensen, H. *et al.* Release of methane from a volcanic basin as a mechanism for initial Eocene global warming. *Nature* **429**, 542–545 (2004).

Supplementary Information is linked to the online version of the paper at www.nature.com/nature.

Acknowledgements This research used samples and data provided by the Ocean Drilling Program (ODP). This work was supported by the Netherlands Organisation for Scientific Research (L.J.L., A.S. and D.K.), Utrecht Biogeology Centre (A.S.), Deutsche Forschungsgemeinschaft (U.R.), and the National Science Foundation (J.C.Z., E.T. and J.B.). We thank the scientific and non-scientific crew of ODP Leg 208, J. Suhonen in particular, and G. Ittman, A. E. van Dijk, G. M. Ganssen, S. J. A. Jung, H. B. Vonhof, P. L. Koch, H. Brinkhuis, F. J. Hilgen, T. Kouwenhoven and J. W. Zachariasse for technical support, advice and comments.

Author Information Reprints and permissions information is available at npg.nature.com/reprintsandpermissions. The authors declare no competing financial interests. Correspondence and requests for materials should be addressed to L.J.L. (llorens@geo.uu.nl).